Published in final edited form as:
Cancer Res. 2014 March 1; 74(5): 1319–1328. doi:10.1158/0008-5472.CAN-13-2768.

A novel radiotracer to image glycogen metabolism in tumors by positron emission tomography

Timothy H. Witney[1], **Laurence Carroll**[1], **Israt S. Alam**[1], **Anil Chandrashekran**[1], **Quang-Dé Nguyen**[1], **Roberta Sala**[1], **Robert Harris**[2], **Ralph J. DeBerardinis**[2], **Roshan Agarwal**[3], and **Eric O. Aboagye**[1]

[1]Comprehensive Cancer Imaging Centre, Department of Surgery and Cancer, Faculty of Medicine, Imperial College London, Hammersmith Hospital, Du Cane Road, London, W12 0NN, UK

[2]Children's Medical Center Research Institute, University of Texas - Southwestern Medical Center at Dallas, Dallas, Texas 75390-9063, USA

[3]Ovarian Cancer Action Research Centre, Department of Surgery and Cancer, Faculty of Medicine, Imperial College London, Hammersmith Hospital, Du Cane Road, London, W12 0NN, UK

Abstract

The high rate of glucose uptake to fuel the bioenergetic and anabolic demands of proliferating cancer cells is well recognized, and exploited with ^{18}F-2-fluoro-2-deoxyglucose positron emission tomography (^{18}F-FDG-PET) to image tumors clinically. In contrast, enhanced glucose storage as glycogen (glycogenesis) in cancer is less well understood and the availability of a non-invasive method to image glycogen *in vivo* could provide important biologic insights. Here, we demonstrate that ^{18}F-*N*-(methyl-(2-fluoroethyl)-1H-[1,2,3]triazole-4-yl)glucosamine (^{18}F-NFTG) annotates glycogenesis in cancer cells and tumors *in vivo*, measured by PET. Specificity of glycogen labeling was demonstrated by isolating ^{18}F-NFTG-associated glycogen and with stable knockdown of glycogen synthase 1, which inhibited ^{18}F-NFTG uptake, while oncogene (*Rab25*) activation-associated glycogen synthesis led to increased uptake. We further show that the rate of glycogenesis is cell cycle-regulated, enhanced during the non-proliferative state of cancer cells. We demonstrate that glycogen levels, ^{18}F-NFTG, but not ^{18}F-FDG uptake, increase proportionally with cell density and G_1/G_0 arrest with potential application in the assessment of activation of oncogenic pathways related to glycogenesis and the detection of post treatment tumor quiescence.

Corresponding Author: Eric Aboagye, Comprehensive Cancer Imaging Centre, Department of Surgery and Cancer, Faculty of Medicine, Imperial College London, Hammersmith Hospital, Du Cane Road, London, W12 0NN, UK. eric.aboagye@imperial.ac.uk. Tel: +44(0)20 3313 3759..

Conflict of interest: The authors declare no conflicts of interest

AUTHORS' CONTRIBUTIONS

T.H.W., R.A. and E.O.A. designed the study and wrote the manuscript. L.C. performed ^{18}F-NFTG radiochemistry and chromatographic analysis. T.H.W., I.S.A., A.C., QD. N., R.S., R.H. and R.J.D. performed biology experiments, with data analyzed by T.H.W.

Keywords

Glycogen; PET; ^{18}F-FDG; ^{18}F-NFTG; Tumor

INTRODUCTION

The majority of tumors exhibit substantially increased levels of glucose uptake and utilization in comparison to non-neoplastic tissues. These tumors use rapid glycolysis and lactate secretion even under normoxic conditions – a phenomenon first reported by Warburg in the 1920s. (reviewed in (1)). This transition - the Warburg effect (2) - provides a selective advantage for tumor growth, progression and protection from death (1, 3-5).

In addition to increased glycolytic flux, tumor cells originating from epithelial tissues also accumulate glycogen (6-8). Initially thought to be limited to specific histotypes such as clear cell cancers, recent data suggest that this is a more generalized phenomenon, with potential prognostic and therapeutic implications (9, 10). Glycogen is a branched glucose polymer, and the principal glucose store in mammalian cells. Glycogen is synthesized from the activated glucose donor, uridine diphosphate glucose (UDP-glucose), catalyzed by glycogen synthase (GS), the key regulatory enzyme in glycogenesis. GS has two isoforms: GYS1 (muscle) and GYS2 (liver) (11), controlled both by allosteric effectors (G-6-P, ATP and AMP) and by inhibitory phosphorylation of GS at multiple sites (12).

Distinct from our perception of the cancer cell as a cell deficient in energy stores requiring glucose uptake and glycolysis to meet energy demands, emerging data suggest that oncogenic signaling and the quiescent state can induce glycogen storage in cancer cells (glycogenesis), and buffer bio-energetic stress. In ovarian cancer, glycogen stores are particularly high in chemoresistant clear cell adenocarcinomas, and the oncogenic small GTPase, Rab25, has recently been shown to increase glycogen stores: resulting in increased resistance to nutrient deprivation induced bio-energetic stress, therapy-induced apoptosis, and poor prognosis (9). In addition, when cancer cells enter the stationary growth phase (quiescence), like budding yeast (13, 14), they synthesize glycogen (or trehalose), with the switch to growth being associated with diminished glycogenesis (6, 7, 15). While the molecular mechanisms responsible for enhanced glycogenesis in mammalian cells are not well understood, it can be appreciated that non-invasive assessment of this metabolic switch could have important applications in cancer. Cytotoxic drugs used in cancer chemotherapy generally cause DNA damage, inhibit DNA replication and/or cell division and are therefore active predominantly in proliferative cycling cells. Quiescent cells in tumors, such as dormant cells following chemotherapy and/or stem cells, therefore exhibit relative chemo-resistance.

It is against this background that we sought to develop a novel non-invasive measure of tissue glycogen for clinical use. Previous methods used to detect glycogen, such as the incorporation of tritiated glucose (16), immuno-cytochemistry (17), or glucose quantification following glycogen hydrolysis (18), are invasive techniques requiring biopsies. These methods also raise concerns regarding sampling a small region, and the ability to generalize to a heterogeneous tumor, that are well documented (19). More

recently, 2-[*N*-(7-nitrobenz-2-oxa-1,3-diazol-4-yl) amino]-2-deoxy-D-glucose (2-NBDG), a fluorescent glucosamine derivative developed to measure cell viability and glucose transport, has been used to quantify glycogen storage in rat hepatocytes in culture (20). Fluorescent imaging of glycogen synthesis by 2-NBDG is ideal for *in vitro* measurements in intact cells, but poor tissue penetration of the emitted green fluorescence precludes its use *in vivo*. The substitution of fluoride in ^{18}F-FDG for the C-2 hydroxyl moiety in glucose prevents metabolism past the second step of glycolysis catalyzed by glucose-6-phosphate isomerase; and ^{18}F-FDG is not incorporated into glycogen. By contrast, we present here a non-invasive method for the *in vivo* detection of glycogen storage by positron emission tomography exploiting a novel glucosamine derivative, ^{18}F-*N*-(methyl(2-fluoroethyl)-1H-[1,2,3]triazole-4-yl))glucosamine (^{18}F-NFTG). ^{18}F-NFTG retains the alpha-proton required for the initial flux into newly formed glycogen, analogous to 2-NBDG (**Fig. 1A**).

MATERIALS & METHODS

Cell culture

IGROV-1 ovarian adenocarcinoma cells were a kind donation from the Institute of Cancer Research (Sutton, Surrey, UK; 2006). Generation of HEY *Rab25*, HEY *pcDNA* and IOSE80ht *pcDNA* cells have been previously described (21) and were obtained from MD Anderson Cancer Center (Houston, TX, USA; 2010). All cells were maintained in RPMI 1640 medium, supplemented with 10% fetal calf serum, 2mM L-glutamine, 100U.mL^{-1} penicillin and 100 μg.mL^{-1} streptomycin (Invitrogen) and were maintained at 37°C in a humidified atmosphere containing 5% CO_2. Regarding cell line authentication, cells were analyzed by short tandem repeat (STR) profiling (DNA Diagnostics Centre) using the Promega PowerPlex Fusion System just prior to publication.

Cell treatments and cell density experiments

The effect of HEY *Rab25* cell density on 2-NBDG fluorescence and glycogen immunostaining was performed in 8-well Lab-Tek chamber slides (TermoFisher Scientific), seeded with 1.25×10^4 cells/cm^2. Measurements were made at 1, 3 and 6 days post seeding. For all other density-dependent measurements, cells were seeded at 12.8×10^4 cells/cm^2, 6.4×10^4 cells/cm^2, 3.2×10^4 cells/cm^2 and 1.6×10^4 cells/cm^2, with analysis performed 24h post seeding.

2-NBDG fluorescence microscopy and quantitation

2-NBDG fluorescence microscopy was performed as previously described (20). Briefly, cells were incubated with 500μM 2-NBDG at 37°C for 3h in complete growth medium in the dark. Cells were washed 3× with warm PBS, followed by fresh warm media. Fluorescence measurements and images were obtained with at 400× magnification on a Zeiss Axiovert S100 inverted microscope (Carl Zeiss Ltd.). For washout experiments, cells were maintained at 37°C and 5% CO_2 within the microscope imaging chamber, with images taken every 20 min.

For fluorescence quantitation, HEY *Rab25* cells were seeded in black 96-well tissue culture plates (ThermoFisher Scientific. Inc.), at cell densities described above. Approximately 24h

post seeding, fresh media containing 500μM 2-NBDG was added to cells. Following 3h incubation, cells were washed 3× with ice-cold PBS and lysed in 50 μL RIPA buffer (Thermo Fisher Scientific Inc.). Fluorescence was subsequently quantified on a PHERAstar^{plus} fluorescence plate reader (BMG LABTECH GmbH; λ Ex/Em=65/540nm) and normalized for protein content using a BCA 96-well plate assay (ThermoFisher Scientific)

Quantification of total cellular glycogen

Total cellular glycogen was evaluated in cells, seeded in 10cm plates for 24h. Cells were subsequently evaluated using a colorimetric Glycogen Assay Kit from Biovision, according to the manufacturer's instructions. Samples were transferred to 96-well plates, with colorimetric measurements read in a Tecan Sunrise plate reader at 570nm. Total cellular glycogen was normalized to protein levels using a BCA assay.

Radiotracer studies

^{18}F-NFTG synthesis and radiolabeling was performed according to previously described methodology (22).

In vitro ^{18}F-NFTG and ^{18}F-FDG cell uptake

Cells were plated into 6-well plates 24h prior to analysis. For non-cell density-dependent measurements, cells were seeded at 2.4×10^5 cells/well of a 6-well plate. 1.0×10^6 cells/well were seeded for GYS1 shRNA experiments. On the day of the experiment, fresh growth medium, containing approximately 0.74MBq ^{18}F-NFTG or ^{18}F-FDG, was added to individual wells (1mL). Cell uptake was measured following incubation at 37°C in a humidified atmosphere of 5% CO_2 for 3h. Plates were subsequently placed on ice, washed 3 times with ice-cold PBS and lysed in RIPA buffer (Thermo Fisher Scientific Inc.; 1mL, 10 min). Cell lysates were transferred into counting tubes and decay-corrected radioactivity was determined on a gamma counter (Cobra II Auto-Gamma counter, Packard Biosciences Co.). Aliquots were snap-frozen and used for protein determination following radioactive decay by a BCA assay. Data were expressed as percent of total radioactivity incorporated into cells, normalized for total cellular protein.

Direct glycogen labeling with ^{18}F-NFTG

For the assessment of direct labeling of pro- and macro-glycogen with ^{18}F-NFTG, 5.9×10^6 HEY *Rab25* cells were seeded in triplicate into 10cm plates. 24h post seeding, ~3.7MBq ^{18}F-NFTG were added to wells and incubated for 3h at 37°C in a humidified atmosphere containing 5% CO_2. Cells were washed 3× with ice-cold PBS and scraped into 1mL of RIPA buffer, 10% TCA or 20% KOH, 65% ethanol for analysis of whole cell lysates, proglycogen and macroglycogen respectively. Cells were lysed following 10× passages in an Ultra-Turrax T-25 homogeniser (IKA Werke GmbH and Co. KG). Aliquots were taken for protein analysis, with glycogen isolation performed as in Huang *et al*. (23). Samples were transferred into counting tubes and decay-corrected radioactivity was determined on a gamma counter. Total glycogen was assessed in samples by the glycogen

colorimetric assay and glycogen-associated radioactivity was expressed as a percentage of radioactivity in whole cell lysates, normalized for glycogen content.

RNA interference

Lentiviral plasmid containing a short-hairpin RNA (shRNA) targeting human *glycogen synthase 1* mRNA was cloned in pLKO1 lentiviral vector (Sigma) using the following sequence: 5'-CCGGCAAGGGCTGCAAGGTGTATTTCTCGAGAAATACACCTTGCAGCCCTTGTT T TTG-3' (TRCN0000045696). Recombinant lentiviruses were generated using a three-plasmid system in 293T cells as previously described (24). Viral titers were determined on 293T cells and target cells (HEY *Rab25*) transduced twice at a multiplicity of infection (MOI) 10. Transduced cells were continuously selected in 1μg/ml puromycin (Sigma). Knockdown of glycogen synthase 1 activity was measured by Western blotting.

DNA cell cycle analysis

DNA-based flow cytometric analysis of cell cycle progression was performed using propidium iodide (PI) in fixed, permeabilized cells according to standard procedures (25). Cells were analyzed in an FACS Canto Cytometer (BD Biosciences), with 10,000 cells counted per treatment.

Western blotting

Rabbit antibody to Rab25, p27 Kip1, glycogen synthase, cdk-4, pRb, phospho-pRB (Ser807/811) and mouse anti-cyclin D1 and cdk-4 (1:1000 dilution; Cell Signaling Technology) were used in a standard western blotting protocol. A rabbit antibody to actin (Sigma-Aldrich Co.; 1:5000) was used as a loading control.

Metabolism experiments

To measure metabolic rates, 7.5×10^5 cells were plated into 6-cm dishes and cultured until 90% confluent. At time 0, the cells were rinsed in PBS, fed with 2mL of the test medium, and cultured. End-point experiments proceeded for 6h, then the medium was collected and analyzed for metabolite abundance. 0.6mL tissue culture medium was processed by an automated chemical analyzer to determine glucose, lactate, glutamine and glutamate concentrations (BioProfile Basic4, NOVA Biomedical). Differences in metabolite concentration between time-0 and end medium were used to calculate rates of nutrient utilization and metabolite excretion, normalized to the cellular protein content of the dish (26).

In vivo tumor models

All animal experiments were performed by licensed investigators in accordance with the United Kingdom Home Office Guidance on the Operation of the Animal (Scientific Procedures) Act 1986 and within published guidelines for the welfare and use of animals in cancer research (27). Female BALB/c nude mice (aged 6–8 weeks; Charles River) were used. HEY *Rab25* or IGROV-1 tumor cells (2×10^6) were injected subcutaneously on the back of mice and animals were used when the xenografts reached ~$100mm^3$. Tumor

dimensions were measured continuously using a caliper and tumor volumes were calculated by the equation: volume = (π/6)×a×b×c, where a, b, and c represent three orthogonal axes of the tumor.

PET imaging studies

Dynamic ^{18}F-NFTG imaging scans were carried out on a dedicated small animal PET scanner (Siemens Inveon PET module, Siemens Medical Solutions USA, Inc.) following a bolus *i.v.* injection of ~3.7MBq of the radiotracer into tumor-bearing mice (28). Dynamic scans were acquired in list mode format over 60 min. The acquired data were then sorted into 0.5 mm sinogram bins and 19 time frames for image reconstruction (4×15s, 4×60s, and 11×300s), which was done by filtered back projection. The Siemens Inveon Research Workplace software was used for visualization of radiotracer uptake in the tumor; 30–60 min cumulative images of the dynamic data were employed to define 3-dimensional (3D) regions of interest (ROIs). Radiotracer blood retention was estimated as in (28). Care was taken to minimize ROI overlap with the myocardium. The count densities were averaged for all ROIs at each time point to obtain a time versus radioactivity curve (TAC). Tumor TACs were normalized to injected dose, ,and expressed as percentage injected dose per mL tissue. The area under the TAC, calculated as the integral of %ID/mL from 0–60 min, and the normalized uptake of radiotracer at 60 min (%ID/mL$_{60}$) were also used for comparisons. For image visualization, iterative reconstruction was performed (3D-OSEM).

Statistical analysis

Data were expressed as mean ± standard deviation (SD) and statistical significance determined using Student's 2-tailed t test. ANOVA was used for multiple comparisons (Prism v5.0 software for windows, GraphPad Software, San Diego, CA, USA). Differences between groups were considered significant if $P \leq 0.05$.

RESULTS

Rab25 overexpression increases punctate 2-NBDG staining and ^{18}F-NFTG uptake

2-NBDG fluorescence microscopy—Addition of 2-NBDG to isogenic HEY *Rab25* and HEY *pcDNA* cells resulted in rapid cellular uptake and retention. The overexpression of Rab25, in HEY *Rab25* cells was confirmed by western blotting (**Fig. 1B**). Washout of diffuse 2-NBDG-derived background fluorescence revealed punctate granular cytosolic fluorescence in both HEY *Rab25* and HEY *pcDNA* cells. The number and intensity of punctate 2-NBDG fluorescent foci were qualitatively higher in *Rab25*-overexpressing HEY cells compared to empty vector HEY *pcDNA* cells, and fluorescence remained up to 4h post removal of 2-NBDG (**Fig. 1C**). In non-tumorigenic immortalized human ovarian epithelial IOSE80ht cells, no punctate staining was observed in IOSE80ht after washout, with intracellular fluorescence lost by 2h (**Fig. 1C**).

Radiosynthesis of ^{18}F-NFTG—We synthesized ^{18}F-NFTG by a copper-catalyzed 1,3-dipolar cycloaddition reaction (22). For *in vivo* PET studies injection-ready ^{18}F-NFTG was obtained from ^{18}F-fluoride with a radiochemical yield of 15%±5% (non-decay-corrected) (22). The radiochemical purity was >98% from n=12 individual syntheses.

Cell uptake of ^{18}F-NFTG - influence of Rab25—Temporal uptake of ^{18}F-NFTG was assessed in HEY *Rab25* and HEY *pcDNA* cells under the same conditions as 2-NBDG. Significantly higher ^{18}F-NFTG uptake was detected in HEY *Rab25* (2.80±0.26% radioactivity/mg protein) compared to HEY *pcDNA* cells at 3h (2.18±0.11% radioactivity/mg protein; *P*=0.019; **Fig. 1D**). A 30% higher ^{18}F-NFTG uptake was observed in HEY *Rab25* in comparison to HEY *pcDNA* cells at 4h post radiotracer addition (3.17±0.25% radioactivity/mg protein and 2.45±0.17% radioactivity/mg protein respectively; *P*=0.014). In HEY Rab25 cells, total cellular glycogen was 51% higher than *pcDNA* control cells (**Fig 1E**), with 2.95±0.53 μg/mg protein and 1.95±0.15 μg/mg protein measured, respectively, consistent with differences in glycogen stores measured previously (9).

Direct labeling of extractable glycogen with ^{18}F-NFTG—Direct labeling of glycogen with ^{18}F-NFTG was shown following glycogen extraction, 3h after HEY *Rab25* cells were exposed to ^{18}F-NFTG. In total, 69.2±2.3% intracellular radioactivity was associated with proglycogen, whereas macroglycogen-labeling was below the limit of detection (**Fig. 1F**).

Glycogen synthase 1 regulates 2-NBDG staining and ^{18}F-NFTG uptake

While the metabolic fate of glucose and glucosamine has been well documented, the effect of their derivatization on metabolic flux is not known. The potential metabolic pathways in which ^{18}F-NFTG is substrate are illustrated in **Fig. 2A,** compared to the known fate of ^{18}F-FDG. To explore the dependence of 2-NBDG and ^{18}F-NFTG cell retention on glycogenesis, HEY *Rab25* cells were transfected with GYS1 shRNA or control lentiviral vector. Greater than 90% knockdown of GYS1 was achieved in the GYS1 shRNA cells in comparison to controls (**Fig. 2B**). Three further GYS1 shRNA sequences produced equivalent target knockdown (**Fig. S1**). GYS1 depletion resulted in a corresponding 5.4-fold reduction in total extractable glycogen (**Fig. 2C**), from 10.4±0.8 μg/mg protein in empty vector (EV) control cells to 1.9±0.1 μg/mg protein in GYS1 shRNA cells (*P*=0.00004; *n*=3). To understand the effect of GYS1 knockdown and resulting glycogen depletion on metabolic pathway flux, cells were grown to confluency in high glucose-containing media (11.11mM), with media subsequently analyzed for glucose and glutamine consumption and the secretion of catabolic by-products (lactate and glutamate). Under these nutrient-rich conditions there was no significant difference between EV control and GYS1 knockdown cells in either glucose or glutamine utilization (**Fig. 2D**).

2-NBDG fluorescence microscopy qualitatively revealed a substantial decrease in staining in GYS1 knockdown cells *versus* EV controls (**Fig. 2E**), consistent with glycogen levels in the two cells, and despite minimal differences in glycolytic flux between the two lines. In contrast, differences in ^{18}F-FDG cellular retention were unremarkable between GYS1 shRNA and EV HEY *Rab25* cells, in keeping with the minimal differences in initial glycolytic flux between the two cell lines. ^{18}F-FDG uptake was reduced by just 9% in GYS1 shRNA cells in comparison to control cells, with 10.2±0.2% radioactivity/mg protein and 11.2±0.6% radioactivity/mg protein measured in cells, respectively (*P*=0.045; **Fig. 2F**). Conversely, knockdown of GYS1 expression resulted in a corresponding 7.3-fold reduction

in ^{18}F-NFTG uptake when compared to EV control cells (7.69±0.68% radioactivity/mg protein and 1.05±0.05% radioactivity/mg protein, respectively; *P*=0.00007; **Fig. 2G**), supporting the utility of substituted glucosamine derivatives, 2-NBDG and ^{18}F-NFTG, to report GS-mediated glycogenesis.

^{18}F-NFTG detects increased glycogen storage induced by G_1/G_0 cell cycle arrest

2-NBDG fluorescence microscopy and anti-glycogen immunofluorescence— High 2-NBDG punctate fluorescence with an anti-glycogen IgM (20, 29). was observed in HEY *Rab25* cells when confluency was achieved in culture, 6 days post seeding (**Fig. S2**). Similarly anti-glycogen immunofluorescence staining of fixed cells also demonstrated granular cytosolic fluorescence, albeit with some non-specific background staining (**Fig. S2**). Overlay of 2-NBDG fluorescence and glycogen immunofluorescence images was not possible as 2-NBDG fluorescence was lost during fixation and permeabilization of cells. We noted in washout experiments a reduction in punctate 2-NBDG staining 40 min prior to cell division in comparison to non-dividing cells; this effect also corresponded to an increase in diffuse background 2-NBDG fluorescence (**Fig. S3**).

Confluency induces G_1/G_0 growth arrest, cellular senescence and glycogen accumulation—The role of growth arrest on glycogen accumulation was further assessed by varying cell seeding density (confluency) from 1.6×10^4 cells/cm^2 to 12.8×10^4 cells/cm^2, 24h prior to analysis. In the asynchronous cultures, increased seeding density resulted in a proportional increase in G_1/G_0 growth arrest, characterized by flow cytometric measurements of DNA content (**Fig. 3A**) and a decrease in phospho-pRb levels (**Fig. 3B**). Furthermore, the quiescence marker, p27/Kip1, and β-galactosidase staining for senescence, were both increased at the highest cell seeding density of 12.8×10^4 cells/cm^2 (**Fig. 3B** and **S4**, respectively), whereas total cyclin D1 levels remained unchanged (**Fig. 3B**). A linear relationship between cell seeding density and total extractable glycogen was observed in HEY *Rab25* cells, increasing from 2.95±0.53 μg/mg protein with the lowest seeding density (1.6×10^4 cells/cm^2) to 6.29±0.75 μg/mg protein at the highest (12.8×10^4 cells/cm^2) – a 2.1-fold increase (*P*=0.0019; *n*=3; **Fig. 3C**). A density-dependent increase in 2-NBDG fluorescence was also observed, rising 2.8-fold, from 229±63 RFU/μg protein to 629±188/μg protein for cells seeded at 1.6×10^4 cells/cm^2 and 12.8×10^4 cells/cm^2, respectively (**Fig. 3D)**.

^{18}F-NFTG and ^{18}F-FDG cellular uptake—Having confirmed an association between confluency (quiescence)-induced glycogen storage and 2-NBDG fluorescence, *in vitro* uptake of ^{18}F-NFTG was performed in HEY *Rab25* cells. An increase in cell density increased tracer uptake and retention. Cells seeded at 1.6×10^4 cells/cm^2 retained 3.51±0.18% radioactivity/mg protein, increasing to 6.63±0.25% radioactivity/mg protein at a density of 6.4×10^4 cells/cm^2 – a 1.9-fold increase (*P*=0.0006; *n*=3). The increase in ^{18}F-NFTG uptake started to plateau at the highest density of 12.8×10^4 cells/cm^2 - 7.69±0.68% radioactivity/mg protein (**Fig. 3E**). Similar experiments were conducted with ^{18}F-FDG, to assess corresponding levels of glucose uptake. Although overall cellular uptake of ^{18}F-FDG was higher in HEY *Rab25* cells in comparison to ^{18}F-NFTG (12.08±0.58% radioactivity/mg protein *versus* 7.69±0.68% radioactivity/mg protein respectively at 12.8×10^4 cells/cm^2; **Fig.**

3F), seeding density did not alter ^{18}F-FDG uptake. When compared, there was good correlation between both 2-NBDG fluorescence and ^{18}F-NFTG uptake with cellular glycogen (R^2=0.9336 and R^2=0.8998, respectively), with no correlation between ^{18}F-FDG and glycogen (R^2=0.0016; **Fig. 3G**).

Increased 2-NBDG uptake is observed in the quiescent core of HEY Rab25 spheroids—To confirm cell cycle-dependent changes in glycogen labeling as a prelude to *in vivo* studies, 2-NBDG confocal microscopy was performed on HEY *Rab25* multicellular tumor spheroids, grown in 3D culture. Tumor cells in the core of spheroids are usually in G_0, with cycling cells closer to the spheroid surface (30). Approximately 20 μm *Z*-stacks of the spheroid (**Fig. S5**) revealed heterogeneous uptake, with maximum fluorescence visualized in the spheroid core, and a further region of high uptake at the rim of the spheroid.

Comparison between ^{18}F-NFTG and ^{18}F-FDG PET imaging *in vivo*

^{18}F-NFTG PET imaging was performed in size-matched HEY *Rab25* xenograft-bearing nude mice and compared to ^{18}F-FDG PET (**Fig. 4**). ^{18}F-NFTG radiotracer distribution was characterized by rapid liver uptake, followed by clearance through the kidney and bladder. Clearance through the intestines was also observed (**Fig. 4A**). While ^{18}F-NFTG did not accumulate in the brain, heart-specific radioactivity was still present at 60 min, accompanied by good tumor uptake and retention (**Fig. 4B**). In comparison, the typical ^{18}F-FDG distribution of high brain, heart, bladder and tumor radioactivity was observed (**Fig. 4C & D**).

The kinetic profiles of tumor retention also varied considerably between the two tracers, as shown by the time versus radioactivity curves (TAC; **Fig. 4E**). Rapid tumor uptake of ^{18}F-NFTG, peaking at 5 min, preceded a slow wash-out of radioactivity over the remaining 55 min. This was contrasted with ^{18}F-FDG, with a maximal tumor radioactivity achieved 15 min post injection, with subsequent stabilization of tumor-associated radioactivity (**Fig. 4E**). Radio-HPLC analysis of plasma ^{18}F-NFTG radioactivity revealed good tracer stability, with 100% of the parent compound still present 15 min post injection (*n*=3 mice; **Fig. S6**). Radiotracer uptake in the tumor was 2.9-fold higher with ^{18}F-FDG than ^{18}F-NFTG 60 min post injection (4.10±0.38% ID/mL and 1.40±0.29% ID/mL respectively; *P*=0.009).

^{18}F-NFTG pharmacokinetics in other major organs varied substantially compared to ^{18}F-FDG. High heart-associated radioactivity, typical of ^{18}F-FDG, was not present with ^{18}FNFTG, with 42.5±5.9 %ID/mL measured with ^{18}F-FDG in comparison to just 4.2±0.3 %ID/mL with ^{18}F-NFTG at 60 min post injection (**Fig. 4F**). Liver ^{18}F-NFTG radioactivity peaked at 5 min, followed by slow clearance, whereas rapid washout from the liver was observed with ^{18}F-FDG, with maximal radioactivity measured <1 min post injection (**Fig. 4G**). A similar profile of rapid extraction from blood and urinary elimination through the kidneys was evident with both radiotracers (**Fig. S7** and **Fig. 4H,** respectively).

A common confound of many oncological PET radiotracers, including ^{18}F-FDG, is their inability to differentiate between neoplastic and inflammatory tissue, leading to reduced specificity (31). Here, we assessed uptake of both ^{18}F-FDG and ^{18}F-NFTG in an aseptic

inflammation (turpentine) model (**Fig. S8**). Turpentine-induced inflammation, confirmed in histological sections stained with H&E, resulted in a 2.7-fold increase (P=0.003) in ^{18}F-FDG uptake in treated *verses* untreated muscle – clearly visible in the 50-60 minute static PET image. Conversely, no significant change in turpentine-treated muscle ^{18}F-NFTG uptake was detectable by either PET or *ex vivo* biodistribution when compared to the untreated control contralateral muscle (P=0.10).

^{18}F-NFTG uptake correlates to glycogen levels *in vitro* and *in vivo*

A panel of 8 human tumor cell lines were assessed for glycogen content (**Fig. S9**). High total cellular glycogen (44.2±14.8 μg/mg protein) was measured in stationary-phase IGROV-1 ovarian carcinoma cells, 4.8-fold higher than in HEY *Rab25* cells (9.30±1.96 μg/mg protein; P=0.01; n=3; **Fig. 5A**) and, thus, were selected for further evaluation. This difference in extractable glycogen correlated well to *in vitro* uptake of ^{18}F-NFTG, which was 12.26±1.97% radioactivity/mg protein and 2.79±0.26% radioactivity/mg protein in IGROV-1 and HEY *Rab25* cells, respectively (4.4-fold increase; P=0.001; n=3; **Fig. 5B**). Similarly, ^{18}F-NFTG uptake in implanted IGROV-1 xenografts *in vivo* was 1.6-fold higher than in HEY *Rab25* tumors (AUC of 122.7±12.3%ID/mL.min^{-1} and 73.7±2.42%ID/mL.min^{-1} respectively; P=0.028), consistent with the higher glycogen levels measured *in vitro*. In contrast to HEY Rab25 xenografts, tumor-associated radioactivity in the higher glycogen content IGROV-1 xenograft was stable between 15 and 60 min (**Fig. 5C & D**).

DISCUSSION

For over 30 years, aberrant glycogen metabolism has been known to be associated with the metabolic reprogramming that occurs in many cancers (7). Although initially thought to be confined to specific histotypes, recent data have shown that this is a general phenomenon. Little is known about the extent of glycogen storage, the mechanisms governing this phenotypic adaptation and role in resistance and poor prognosis. In this study, we unequivocally demonstrate that measurements of ^{18}F-NFTG uptake and retention can be used to detect *de novo* glycogenesis in tumor cells growing in culture or in tumor xenografts *in vivo*, and that the ^{18}F-NFTG readout of glycogenesis could be used to assess the proliferative state of cancer cells.

Recently, the phosphatidylinositol 3-kinase (PI3K) signaling pathway has been suggested as a key regulator of glycogenesis, linked to increased expression of the small GTPase, Rab25 (9). In Rab25 overexpressing cells, AKT activity was increased, leading to an augmentation of GSK3 phosphorylation and subsequent inactivation. In these cells GSK3 was unable to phosphorylate and therefore inhibit GS activity, resulting in increased glycogen accumulation. Furthermore, it was shown that inhibition of PI3K abrogated Rab25-mediated glycogen storage. 2-NBDG and ^{18}F-NFTG were able to discriminate between small differences in glycogen synthesis in HEY cells induced by Rab25 transfection, and suggest potential utility as a measure of oncogenic signaling-induced changes in glycogen. A measure of oncogene-driven glycogen status may be of prognostic significance, given that Rab25 appears to confer a functional survival advantage to cancer cells; allowing cellular survival under acute nutrient stress conditions (9).

In cell experiments, specificity of glycogen labeling with 2-NBDG was demonstrated by comparison with anti-glycogen immunofluorescence and through extraction of ^{18}F-NFTG-labeled proglycogen. Glycogen labeling by these substituted glucosamine derivatives was proposed via the putative signaling pathway illustrated in **Fig. 2A**, controlled by the key regulator of glycogenesis, glycogen synthase. To further elucidate the specificity of these tracers to report glycogenesis, specific knockdown of muscle glycogen synthase 1 by shRNA was employed. GYS1 knockdown depleted intracellular glycogen stores, reduced ^{18}F-NFTG uptake over 7-fold when compared to empty vector control cells and similarly reduced 2-NBDG retention. Furthermore, GYS1 silencing had no effect on glycolytic flux, ruling out non-specific metabolic effects of GYS1 silencing or off-target toxicities of the shRNA. As expected, ^{18}F-FDG was unable to annotate the glycogen status of these cells. It is important to note that although complementary, measurements of the total intracellular glycogen pool (measured biochemically) and rate of glycogen synthesis (measured by ^{18}F-NFTG) differ: the total glycogen pool is a sum of both glycogenesis and glycogenolysis, whereas ^{18}F-NFTG has only been shown to measure GS-mediated glycogenesis. Future studies are required to elucidate whether ^{18}F-NFTG-associated glycogen is substrate for glycogen breakdown by glycogen phosphorylase.

We examined whether modulation of glycogen storage during the non-proliferative state of cancer cells could be detected by 2-NBDG and ^{18}F-NFTG. Induction of G_0/G_1 growth arrest *in vitro* by increased cell density resulted in an increase in glycogen storage, proportional to the initial cell seeding concentration. In cells, G_0/G_1 arrest led to increased 2-NBDG and ^{18}F-NFTG uptake, whereas ^{18}F-FDG retention remained unchanged. The mechanism behind this increased glycogen storage remains to be fully determined. We speculate that the high ^{18}F-FDG/glucose uptake attributed to the Warburg effect aims to provide the building blocks for cellular proliferation through, for example, the pentose phosphate shunt, whereas in quiescent tumor cells the excess glucose is instead diverted to glycogen. This could then be potentially mobilized when the cell re-enters cell cycle for both energy and as a carbon source for the synthesis of proteins, nucleotides and other building blocks; analogous to nutrient stress-induced quiescence, and synthesis of glycogen and trehalose by budding yeast (13, 14).

To provide further evidence for uptake of the substituted glucosamines in the quiescent state, we used a more sophisticated model of heterogeneous tumor cell growth - multicellular tumor spheroids (reviewed in (30)). In this model, we revealed elevated 2-NBDG uptake in the hypoxic spheroidal core, where cells are relatively quiescent (32) and express elevated GYS1 (10). The high uptake of 2-NBDG in the rim of the spheroid may reflect improved nutrient, and therefore 2-NBDG, access in this region. While our focus has been on glycogenesis, it should be noted that other mechanisms could be responsible for the high glycogen levels in quiescent cells. For instance, it was shown recently that inhibition of glycogen phosphorylase activity and glycogenolysis in cancer leads to a p53-dependent induction of senescence, providing a mechanistic link between cellular glycogen and senescence (10). The ability to non-invasively measure tumor proliferative state, be it cellular quiescence or senescence may be of great importance.

Given the ability of ^{18}F-NFTG-PET to measure cellular glycogen levels as a metabolic biomarker of oncogene activation (e.g. PI3K/AKT pathway by Rab25), and G_1/G_0 quiescence, we envisage that ^{18}F-NFTG-PET could potentially be used to complement ^{18}F-FDG-PET imaging of tumor glycolysis. Dynamic imaging revealed distinct patterns of ^{18}F-NFTG tissue retention in comparison to ^{18}F-FDG, characterized by high uptake in the kidneys and in glycogen-storing liver. As the liver is a frequent site of metastasis, this could limit the utility ^{18}F-NFTG in these patients. However, some tumors are not ^{18}F-FDG avid due to low metabolic rates. These are frequently slow growing tumors. Based on the relationship between cell cycle and glycogen levels, ^{18}F-NFTG could complement ^{18}F-FDG in imaging of such tumors. In oncology ^{18}F-FDG-PET is also used as a marker of treatment response. ^{18}F-FDG can overestimate the efficacy of cytotoxic chemotherapy due to a stunning effect, resulting from a reduction in metabolism due to cellular ‘stress’, or quiescence of residual cells. The potential ability of ^{18}F-NFTG to specifically image these quiescent cells may be an advantage. Furthermore, ^{18}F-NFTG provides improved specificity over ^{18}F-FDG for tumor imaging under conditions of inflammation. We envisage ^{18}F-NFTG to have great applicability to image tumors of the upper thoracic, for example those of the breast, where background is minimal. Utility in ovarian cancer, as depicted in this study, is also envisaged.

We believe that this technique can be successfully transferred to the clinic, with potential application in both malignant and non-malignant diseases; in malignant disease the tracer may have a role in the assessment of activation of oncogenic pathways related to glycogenesis, their modulation by drugs in development, and the detection of post treatment quiescent residual tumor burden.

Supplementary Material

Refer to Web version on PubMed Central for supplementary material.

Acknowledgments

We would like to thank W. Gsell and J. Tremoleda for their assistance with the PET imaging studies, R. Harris for assistance with metabolism experiments, and K. Cheng and G. Mills for the HEY *Rab25*/*pcDNA* and IOSE80ht cell lines.

Financial support: This work was funded by Cancer Research UK–Engineering and Physical Sciences Research Council grant (in association with the Medical Research Council and Department of Health (England)) grant C2536/A10337. E.O.A's laboratory receives core funding from the UK Medical Research Council (MC_A652_5PY80). R.A is funded by a Cancer Research UK Clinician Scientist Fellowship. R.J.D. is supported by the N.I.H. (R01 CA157996-02) and Robert A. Welch Foundation (I-1733).

REFERENCES

1. Gatenby RA, Gillies RJ. Why do cancers have high aerobic glycolysis? Nat Rev Cancer. 2004; 4:891–9. [PubMed: 15516961]
2. Warburg O. On the origin of cancer cells. Science. 1956; 123:309–14. [PubMed: 13298683]
3. Fantin VR, St-Pierre J, Leder P. Attenuation of LDH-A expression uncovers a link between glycolysis, mitochondrial physiology, and tumor maintenance. Cancer Cell. 2006; 9:425–34. [PubMed: 16766262]

4. Herst PM, Hesketh EL, Ritchie DS, Berridge MV. Glycolytic metabolism confers resistance to combined all-trans retinoic acid and arsenic trioxide-induced apoptosis in HL60rho0 cells. Leuk Res. 2008; 32:327–33. [PubMed: 17580091]
5. Simonnet H, Alazard N, Pfeiffer K, Gallou C, Beroud C, Demont J, et al. Low mitochondrial respiratory chain content correlates with tumor aggressiveness in renal cell carcinoma. Carcinogenesis. 2002; 23:759–68. [PubMed: 12016148]
6. Rousset M, Chevalier G, Rousset JP, Dussaulx E, Zweibaum A. Presence and cell growth-related variations of glycogen in human colorectal adenocarcinoma cell lines in culture. Cancer Res. 1979; 39:531–4. [PubMed: 761227]
7. Rousset M, Zweibaum A, Fogh J. Presence of glycogen and growth-related variations in 58 cultured human tumor cell lines of various tissue origins. Cancer Res. 1981; 41:1165–70. [PubMed: 7459858]
8. Takahashi S, Satomi A, Yano K, Kawase H, Tanimizu T, Tuji Y, et al. Estimation of glycogen levels in human colorectal cancer tissue: relationship with cell cycle and tumor outgrowth. J Gastroenterol. 1999; 34:474–80. [PubMed: 10452680]
9. Cheng KW, Agarwal R, Mitra S, Lee JS, Carey M, Gray JW, et al. Rab25 increases cellular ATP and glycogen stores protecting cancer cells from bioenergetic stress. EMBO Mol Med. 2012; 4:125–41. [PubMed: 22253197]
10. Favaro E, Bensaad K, Chong MG, Tennant DA, Ferguson DJ, Snell C, et al. Glucose utilization via glycogen phosphorylase sustains proliferation and prevents premature senescence in cancer cells. Cell Metab. 2012; 16:751–64. [PubMed: 23177934]
11. Roach PJ, Cheng C, Huang D, Lin A, Mu J, Skurat AV, et al. Novel aspects of the regulation of glycogen storage. J Basic Clin Physiol Pharmacol. 1998; 9:139–51. [PubMed: 10212831]
12. Lawrence JC Jr, Roach PJ. New insights into the role and mechanism of glycogen synthase activation by insulin. Diabetes. 1997; 46:541–7. [PubMed: 9075792]
13. Paalman JW, Verwaal R, Slofstra SH, Verkleij AJ, Boonstra J, Verrips CT. Trehalose and glycogen accumulation is related to the duration of the G1 phase of Saccharomyces cerevisiae. FEMS Yeast Res. 2003; 3:261–8. [PubMed: 12689634]
14. Shi L, Sutter BM, Ye X, Tu BP. Trehalose is a key determinant of the quiescent metabolic state that fuels cell cycle progression upon return to growth. Mol Biol Cell. 2010; 21:1982–90. [PubMed: 20427572]
15. Rousset M, Dussaulx E, Chevalier G, Zweibaum A. Growth-related glycogen levels of human intestine carcinoma cell lines grown in vitro and in vivo in nude mice. J Natl Cancer Inst. 1980; 65:885–9. [PubMed: 6933258]
16. Agbanyo M, Taylor NF. Incorporation of 3-deoxy-3-fluoro-D-glucose into glycogen and trehalose in fat body and flight muscle in Locusta migratoria. Biosci Rep. 1986; 6:309–16. [PubMed: 3524699]
17. Graf R, Klessen C. Glycogen in pancreatic islets of steroid diabetic rats. Carbohydrate histochemical detection and localization using an immunocytochemical technique. Histochemistry. 1981; 73:225–32. [PubMed: 7035407]
18. Carr RS, Neff JM. Quantitative semi-automated enzymatic assay for tissue glycogen. Comp Biochem Physiol B. 1984; 77:447–9. [PubMed: 6425007]
19. Marusyk A, Almendro V, Polyak K. Intra-tumour heterogeneity: a looking glass for cancer? Nat Rev Cancer. 2012; 12:323–34. [PubMed: 22513401]
20. Louzao MC, Espina B, Vieytes MR, Vega FV, Rubiolo JA, Baba O, et al. “Fluorescent glycogen” formation with sensibility for in vivo and in vitro detection. Glycoconj J. 2008; 25:503–10. [PubMed: 17973187]
21. Cheng KW, Lahad JP, Kuo WL, Lapuk A, Yamada K, Auersperg N, et al. The RAB25 small GTPase determines aggressiveness of ovarian and breast cancers. Nat Med. 2004; 10:1251–6. [PubMed: 15502842]
22. Carroll L, Witney TH, Aboagye EO. Design and synthesis of novel ^{18}F-radiolabelled glucosamine derivatives for cancer imaging. Med Chem Commun. 2013; 4:653–6.

23. Huang M, Lee C, Lin R, Chen R. The exchange between proglycogen and macroglycogen and the metabolic role of the protein-rich glycogen in rat skeletal muscle. J Clin Invest. 1997; 99:501–5. [PubMed: 9022084]
24. Howe SJ, Chandrashekran A. Vector systems for prenatal gene therapy: principles of retrovirus vector design and production. Methods Mol Biol. 2012; 891:85–107. [PubMed: 22648769]
25. Crissman HA, Hirons GT. Staining of DNA in Live and Fixed Cells. Methods Cell Biol. 1994; 41:195–209. [PubMed: 7532262]
26. Yang C, Sudderth J, Dang T, Bachoo RM, McDonald JG, DeBerardinis RJ. Glioblastoma cells require glutamate dehydrogenase to survive impairments of glucose metabolism or Akt signaling. Cancer Res. 2009; 69:7986–93. [PubMed: 19826036]
27. Workman P, Aboagye EO, Balkwill F, Balmain A, Bruder G, Chaplin DJ, et al. Guidelines for the welfare and use of animals in cancer research. Br J Cancer. 2010; 102:1555–77. [PubMed: 20502460]
28. Witney TH, Alam IS, Turton DR, Smith G, Carroll L, Brickute D, et al. Evaluation of deuterated 18F- and 11C-labeled choline analogs for cancer detection by positron emission tomography. Clin Cancer Res. 2012; 18:1063–72. [PubMed: 22235095]
29. Baba O. [Production of monoclonal antibody that recognizes glycogen and its application for immunohistochemistry]. Kokubyo Gakkai Zasshi. 1993; 60:264–87. Japanese. [PubMed: 8345245]
30. Kunz-Schughart LA, Kreutz M, Knuechel R. Multicellular spheroids: a three-dimensional in vitro culture system to study tumour biology. Int J Exp Pathol. 1998; 79:1–23. [PubMed: 9614346]
31. Yamada S, Kubota K, Kubota R, Ido T, Tamahashi N. High accumulation of fluorine-18-fluorodeoxyglucose in turpentine-induced inflammatory tissue. J Nucl Med. 1995; 36:1301–6. [PubMed: 7790960]
32. Carlsson J, Acker H. Relations between pH, oxygen partial pressure and growth in cultured cell spheroids. Int J Cancer. 1988; 42:715–20. [PubMed: 3182108]

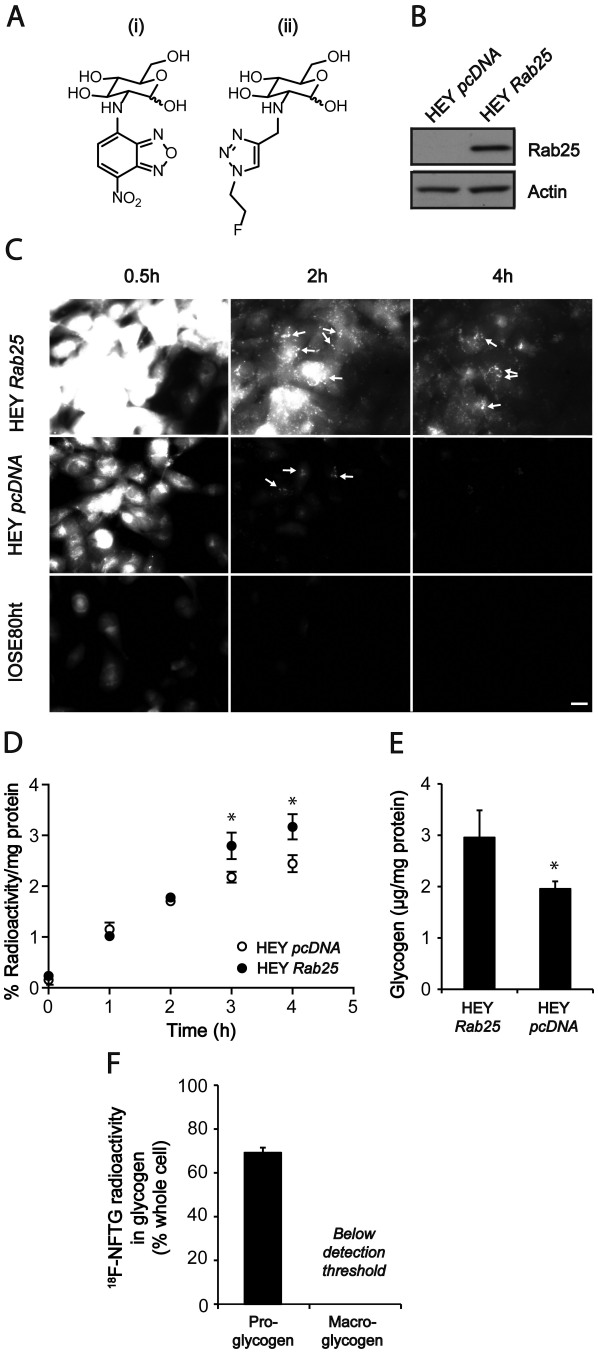

Figure 1.

Effect of *Rab25* oncogene overexpression on 2-NBDG and ^{18}F-NFTG cellular accumulation. *A*, Chemical structures of 2-NBDG (i) and NFTG (ii). *B*, Representative western blot of Rab25 expression in HEY *pcDNA* and HEY *Rab25* cell lines. Actin was used as a loading control. *C*, Fluorescent microscopy images of intracellular 2-NBDG fluorescence in HEY *Rab25*, HEY *pcDNA* and IOSE80ht cells. Images were acquired at the given time points post 2-NBDG removal. Scale bar = 20 µm. *Arrows* point to representative accumulations of punctate fluorescent labeling. All images were acquired at 400×

magnification and are representative of three independent experiments. *D*, Time course of ^{18}F-NFTG uptake *in vitro* in HEY *Rab25* (closed circles) and HEY *pcDNA* (open circles) cancer cell lines. *E*, Total cellular glycogen in *HEY Rab25* and HEY *pcDNA* cells. *F*, ^{18}F-NFTG radioactivity in glycogen. Direct ^{18}F-NFTG labeling of pro- and macro-glycogen isolated from HEY Rab25 cells 3h post radiotracer addition. Counts were normalized for extracted glycogen and presented as a percentage of radioactivity of non-extracted whole cell lysates. Mean values ± SD are shown ($n = 3$; * $P < 0.05$).

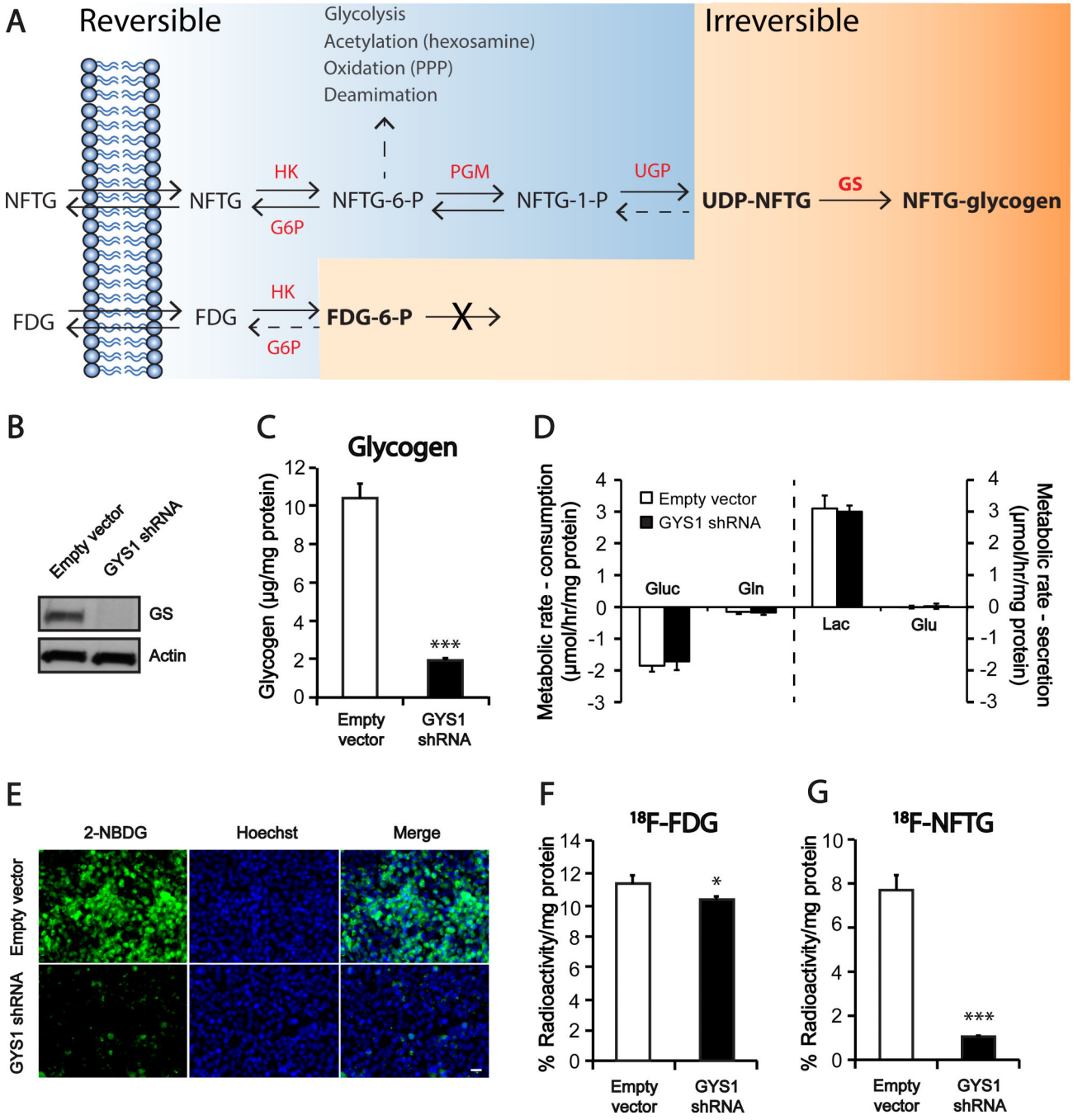

Figure 2.

^{18}F-NFTG and 2-NBDG cellular retention is controlled by the glycogenic enzyme glycogen synthase 1. The enzymes involved in NFTG and FDG metabolism are depicted as well as the signaling pathways that regulate them. *A*, Putative metabolic fates of NFTG and known fate of FDG. The readily-reversible and irreversible intracellular trapping steps are depicted. *B*, Glycogen Synthase 1 knockdown by shRNA in HEY *Rab25* cells. *C*, Changes in total cellular glycogen in relation to GYS1 status. *D*, Metabolic rates in GYS1 knockdown and control cells. *E*, Intracellular 2-NBDG accumulation in Empty vector and GYS1 shRNA

cells. Scale bar = 20 μm. *F*, Effect of GYS1 shRNA on ^{18}F-FDG uptake. *G*, Effect of GYS1 shRNA on ^{18}F-NFTG uptake. Mean values (bars, SD) are shown (n = 3; * P < 0.05; *** P < 0.0001). Abbreviations: NFTG, F-*N*-(methyl(2-fluoroethyl)-1H-[1,2,3]triazole-4-yl))glucosamine; NFTG-6-P, NFTG-6-phosphate; NFTG-1-P, NFTG-1-phosphate; UDPNFTG, uridine diphosphate NFTG; NFTG-glycogen, NFTG-associated glycogen; G6P, glucose 6-phosphatase; HK, hexokinase; PGM, phosphoglucomutase; GS, glycogen synthase; FDG, 2-fluoro-2-deoxyglucose, FDG-6-P, FDG 6-phosphate; GYS1, glycogen synthase 1; Gluc, glucose; Gln, glutamine; Lac, lactate; Glu, glutamate.

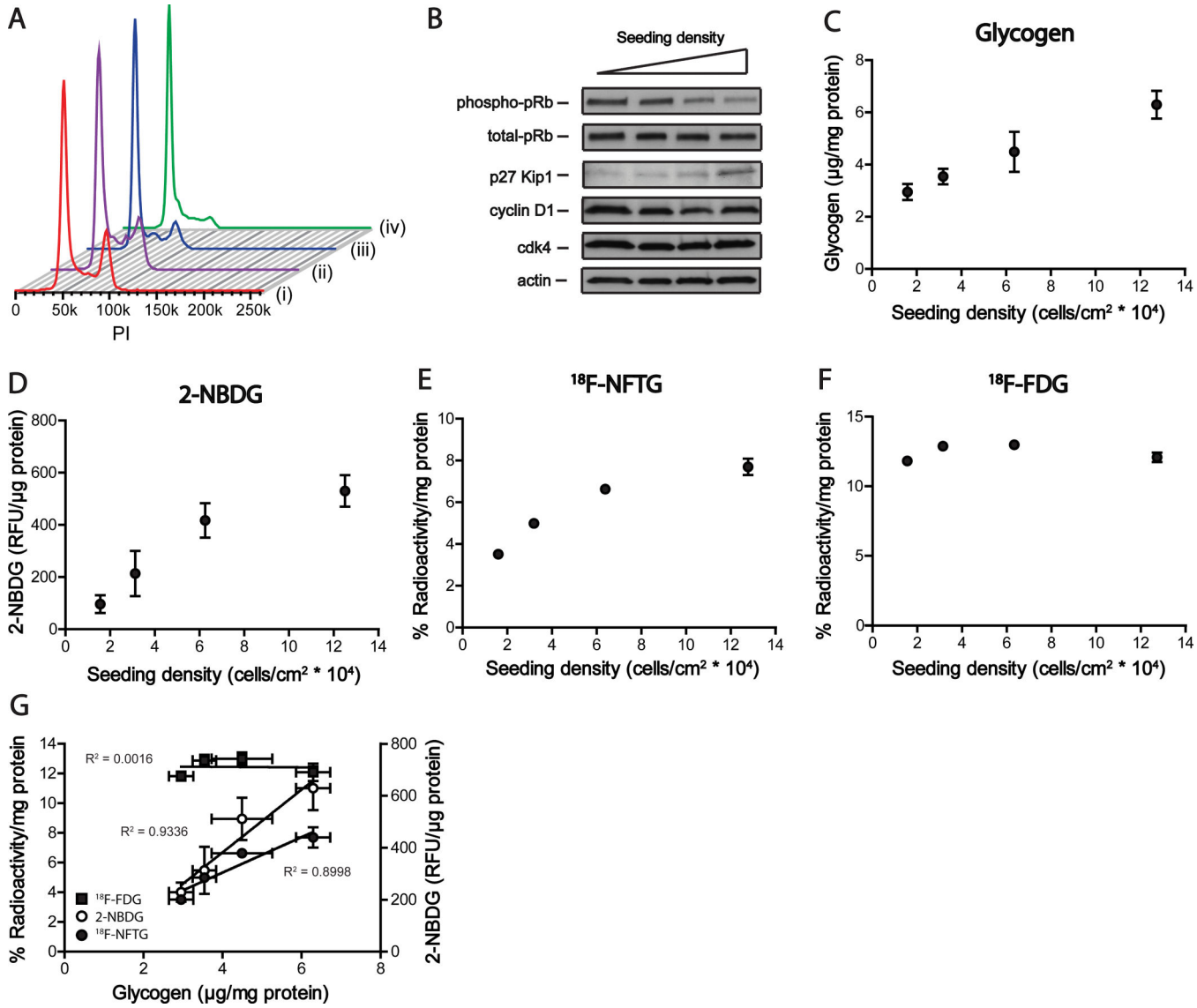

Figure 3.

Variations in intracellular glycogen storage and labeling as a measurement of cell density-dependent HEY *Rab25* G_1/G_0 arrest. *A*, Representative cell cycle plots indicating DNA content are shown for cells seeded in a 6-well plate at 1.5×10^5 cells/well (i), 3×10^5 cells/well (ii), 6×10^5 cells/well (iii) and 1.2×10^6 cells/well (iv). *B*, Western blots for HEY *Rab25*, cultured at seeding densities at 1.5×10^5 cells/well (i), 3×10^5 cells/well (ii), 6×10^5 cells/well (iii) and 1.2×10^6 cells/well (iv) were probed with antibodies against cell cycle control proteins, as indicated. Antibody to actin is shown as a loading control. *C*, Changes in total cellular glycogen in relation to HEY *Rab25* seeding density. *D*, Relation between cell seeding density and total 2-NBDG. *E*, Normalized ^{18}F-NFTG uptake and retention relative to cell seeding density. *F*, Normalized ^{18}F-FDG uptake and retention relative to cell seeding density. (*C–F*), Mean values ± SD are shown ($n = 3$). *G*, Correlation between total cellular glycogen and 2-NBDG fluorescence (open circles), ^{18}F-NFTG uptake (closed circles)

or ^{18}F-FDG uptake (closed squares). All images were acquired at 100× magnification and are representative of three independent experiments.

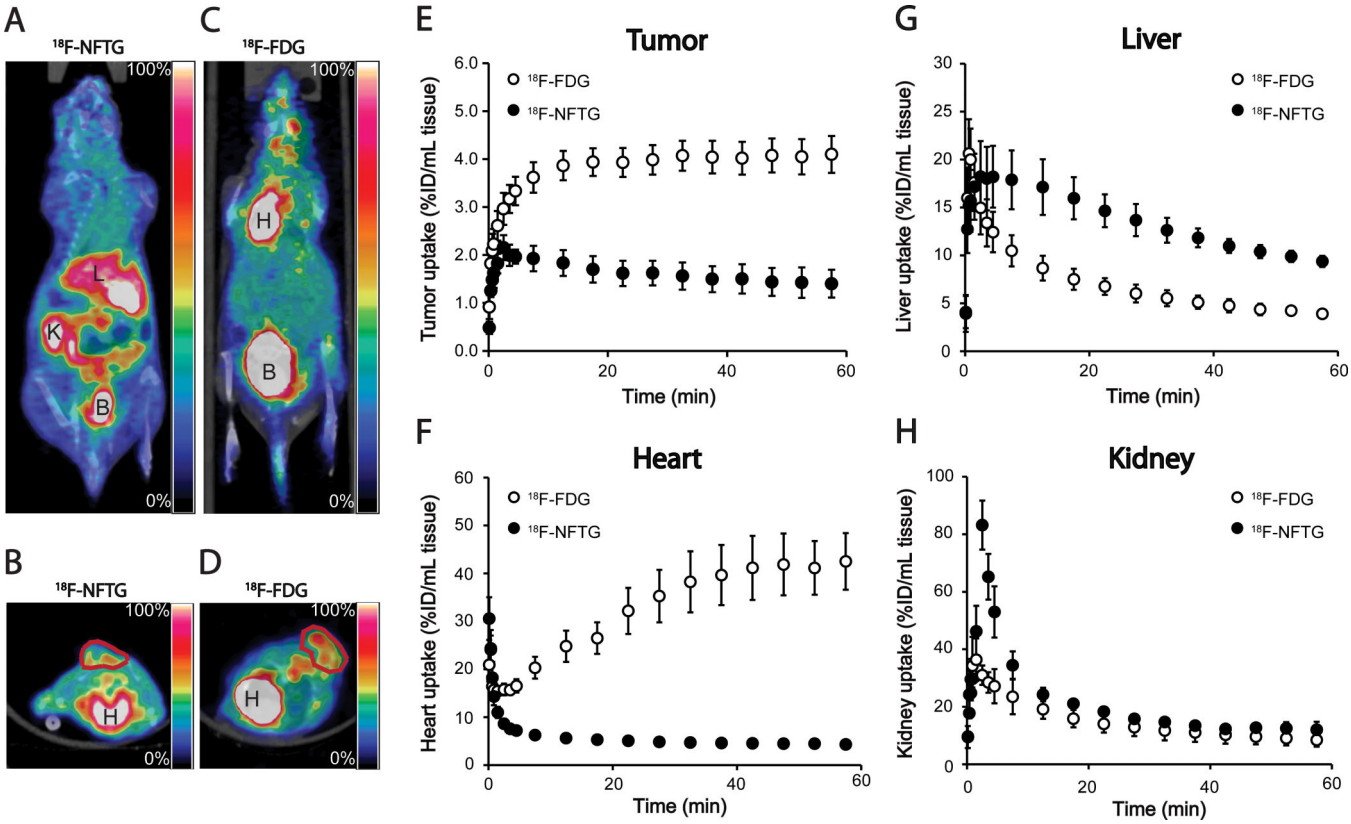

Figure 4.

Dynamic ^{18}F-NFTG and ^{18}F-FDG-PET image analysis in HEY *Rab25* tumor-bearing mice. *A & C*, Representative coronal PET-CT images (30–60 minutes summed activity) for ^{18}F-NFTG (*A*) and ^{18}F-FDG (*C*). Slices were selected to represent key organs with high radiotracer retention. Abbreviations: H, heart; L, liver; K, kidney; B, bladder. *B & D*, Representative axial PET-CT images of HEY *Rab25* tumors (30–60 minutes of summed activity) for ^{18}F-NFTG (*B*) and ^{18}F-FDG (*D*). The slice selected in (*D*) was chosen to minimize background heart radioactivity. Tumor margins, indicated from CT image, are outlined in red. For all images, the color scale was adjusted to the maximum pixel intensity. *E*, HEY *Rab25* tumor time versus radioactivity curve (TAC) obtained from 60-minute dynamic PET imaging. Mean ± SD (n = 4 mice per group). *F*, ^{18}F-NFTG and ^{18}F-FDG heart TAC. *G*, ^{18}F-NFTG and ^{18}F-FDG liver TAC. *H*, ^{18}F-NFTG and ^{18}F-FDG kidney TAC. Mean ± SD (n = 4 mice per group).

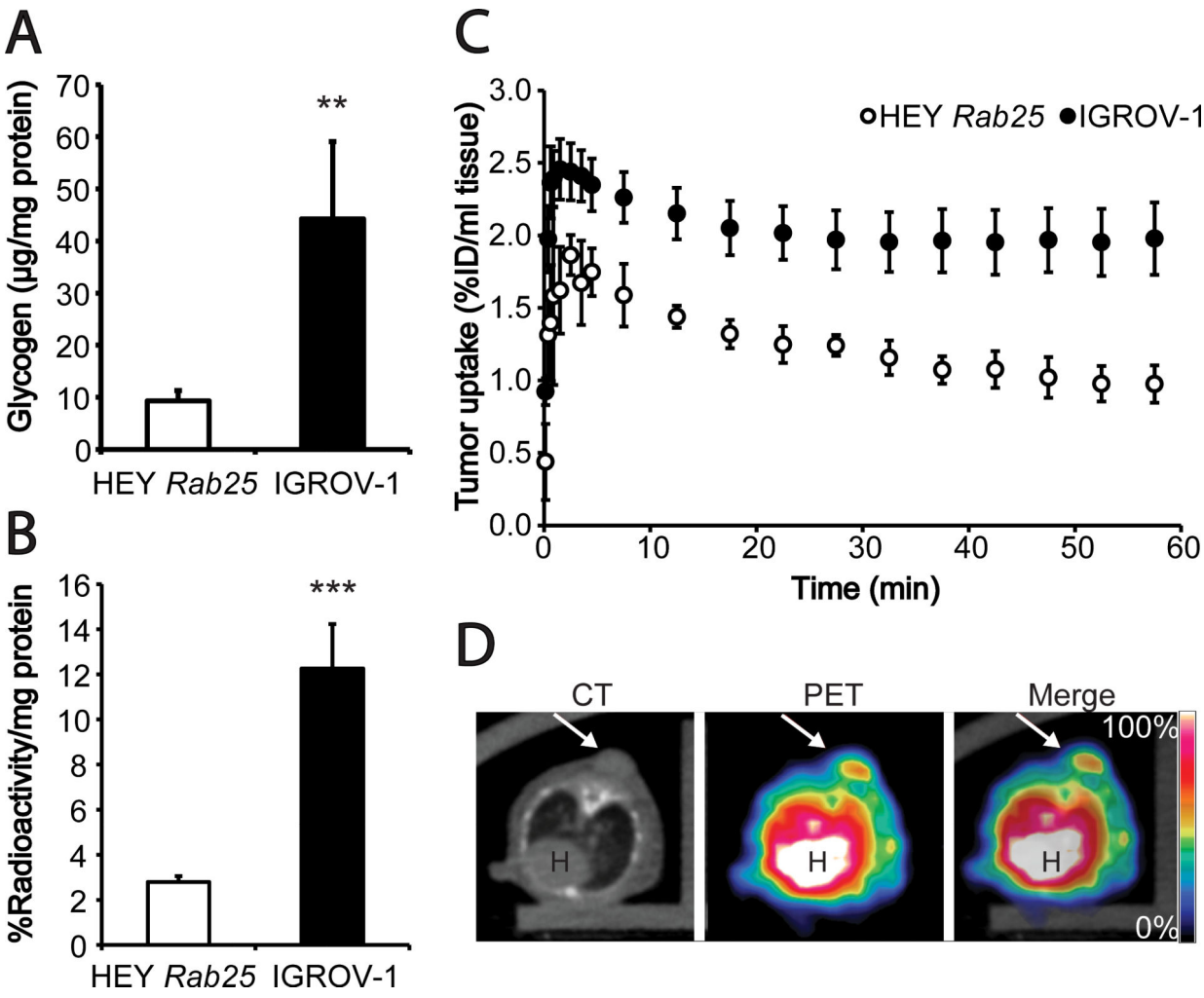

Figure 5.

^{18}F-NFTG uptake in IGROV-1 cells *in vitro* and tumors *in vivo*. *A*, A comparison of total extractable glycogen taken from HEY *Rab25* and IGROV-1 cells grown *in vitro*. *B, In vitro* ^{18}F-NFTG uptake in HEY *Rab25* and IGROV-1 cells. Mean ± SD for *A & B* (n = 3; ** $P < 0.01$; *** $P < 0.001$). *C*, IGROV-1 tumor TAC obtained from 60-minute dynamic ^{18}F-NFTG-PET imaging. Tumor TAC from HEY *Rab25* xenografts are included for comparison. Mean ± SD. (n = 4 mice per group). *D*, Representative axial CT, PET and PETCT images of IGROV-1 tumor-bearing mice (30–60 minutes of summed activity). Tumor margins were identified from CT image (indicated by arrow). Abbreviations: H, heart.